

Disease-Associated Mutations in Human BICD2 Hyperactivate Motility of Dynein-Dynactin

Walter Huynh and Ronald D. Vale

Department of Cellular and Molecular Pharmacology and the Howard Hughes Medical Institute,
University of California, San Francisco, San Francisco, California, USA.

Corresponding Author:

Ronald D. Vale
Dept. of Cellular and Molecular Pharmacology
University of California, San Francisco
Genentech Hall, MC 2200, Room N312A
600-16th Street
San Francisco, CA 94158-2517
E-mail: ron.vale@ucsf.edu
Phone: 415-476-6380
Fax: 415-514-4412

Abstract

Bicaudal D2 (BICD2) joins dynein with dynactin into a ternary complex (termed DDB) capable of processive movement. Point mutations in the BICD2 gene have been identified in patients with a dominant form of spinal muscular atrophy, but how these mutations cause disease is unknown. To investigate this question, we have developed in vitro motility assays with purified DDB and BICD2's membrane vesicle partner, the GTPase Rab6a. Rab6a-GTP, either in solution or bound to artificial liposomes, released BICD2 from an autoinhibited state and promoted robust dynein-dynactin transport. In these assays, BICD2 mutants showed an enhanced ability to form motile DDB complexes. Increased retrograde transport by BICD2 mutants also was observed in vivo using an inducible organelle transport assay. When overexpressed in rat hippocampal neurons, the hyperactive BICD2 mutants decreased neurite growth. Our results reveal that dominant mutations in BICD2 hyperactive DDB motility and suggest that an imbalance of minus- versus plus-end-directed microtubule motility in neurons may underlie spinal muscular atrophy.

Introduction

Eukaryotic cells rely on the activities of plus- and minus-end-directed microtubule motors for proper function and maintenance. The retrograde motor, cytoplasmic dynein, is involved in a host of cellular activities, including the trafficking of diverse cargos such as organelles, vesicles, and mRNA as well as mitotic spindle alignment and chromosome positioning (Allan, 2011). In contrast to yeast dynein, which can achieve long-range transport on its own (Reck-Peterson et al., 2006), mammalian dynein must form a tripartite complex with the 1.2 mDa dynactin complex and an adapter protein to move processively along microtubules (McKenney et al., 2014; Schlager et al., 2014a).

A number of different adaptor proteins that join dynein and dynactin into an active motile complex have been identified (McKenney et al., 2014; Cianfrocco et al., 2015). In addition to enabling the formation of a dynein-dynactin complex, these adaptors bind to receptors located on distinct cargos within the cell. For example, Bicaudal D2 (BICD2), one of best studied dynein adaptors, interacts with the small GTPase Rab6, which is found on early endosomes and ER-Golgi vesicles (Matanis et al., 2002). Rab6 also may play an important role in regulating the ability of BICD2 to interact with dynein and dynactin. BICD2 is thought to be auto-inhibited through an interaction between its C-terminal coiled-coil domain (CC3) with the N-terminal domain of the protein, which prevents it from associating with its other partners, including dynein (Matanis et al., 2002; Hoogenraad et al., 2003; Liu et al., 2013). Auto-inhibition is thought to be relieved by binding to an effector, such as Rab6a in its GTP-bound form (Liu et al., 2013); however, evidence for this model is lacking.

BICD2 recently emerged as a genetic locus associated with spinal muscular atrophy (SMA), a genetic disorder characterized by the degeneration of anterior horn cells and leading to eventual

muscle atrophy and weakness. The most common form of SMA is recessive in nature and is caused by mutations in the survival motor neuron gene, affecting 1 in 10,000 live births each year (Dimitriadi et al., 2016). Genetically dominant forms of the disease also have been identified. Recent studies on autosomal-dominant congenital spinal muscular atrophy (DCSMA) have identified a handful of mutations in BICD2 that are associated with the disease (Neveling et al., 2013; Oates et al., 2013; Peeters et al., 2013). The effects that these point mutations have on BICD2's ability to function as a dynein adaptor are not known, although overexpression of these mutants has been reported to cause Golgi fragmentation and changes in BICD2 localization in cultured cells (Neveling et al., 2013; Peeters et al., 2013). Interestingly, point mutations in the tail region of heavy chain 1 of cytoplasmic dynein have been associated with another form of spinal muscular atrophy, SMA-LED1. These mutations were reported to cause an increase in the affinity between the motor and BICD2 (Peeters et al., 2015) and a decrease in dynein-dynactin processivity (Hoang et al., 2017).

Here, we utilize a combination of biochemical and single-molecule in vitro motility assays to compare the behaviors of wild-type and mutant BICD2. We demonstrate that Rab6a in its GTP-bound form enhances the formation of motile mammalian dynein/dynactin/BICD2 (DDB) complexes. BICD2 mutations associated with human disease cause a gain-of-function in motility, allowing more DDB complexes to form and move along microtubules both in vitro and in vivo. In addition, we show that the expression of BICD2 mutants in neurons leads to impaired neurite outgrowth. These results indicate that the SMA BICD2 mutants hyperactivate dynein motility, a gain-of-function consistent with a dominant genetic trait. An increase in retrograde over anterograde transport in neurons could explain the gradual loss of motor neuron function in SMA.

Results

Activation of BICD2 via Rab6a-GTP increases dynein-dynactin binding and motility

Bicaudal D2 is comprised of five coiled-coil domains that can be grouped into three distinct regions (Fig. 1A). The C-terminal region of the protein is the most well-conserved and contains the binding site to different partners localized to different cargos, including the small GTPase Rab6a (Matanis et al., 2002). The N-terminal construct of the protein, which spans residues 25-400 and includes all of coiled-coil 1 (CC1) and part of CC2 (BICD2₂₅₋₄₀₀), was shown to be more effective in binding dynein-dynactin in cell lysate pull-down assays compared to autoinhibited full-length protein (BICD2_{FL}) (Splinter et al., 2012; McKenney et al., 2014). We replicated these findings; the difference in dynactin binding was especially striking, exhibiting about a 10-fold reduction for the BICD2_{FL} pull-down compared with BICD2₂₅₋₄₀₀, while dynein was ~2-3 fold lower (Supp. Fig. 1A and 1B).

We next tested whether the auto-inhibited state of BICD2_{FL} could be activated by Rab6a. We added purified recombinant Rab6a-Q72L, which is locked in a GTP-bound state (hereon referred to as Rab6a^{GTP}), to porcine brain lysate and performed pull-downs using BICD2 as bait (Matanis et al., 2002). With increasing Rab6a^{GTP}, there was a corresponding increase in the amount of dynein and dynactin in the BICD2_{FL} pulldown (Fig. 1B). Conversely, the GDP-bound mutant of Rab6a (Rab6a^{GDP}) appeared to somewhat reduce the amount of dynein and dynactin recruited from the brain lysate (Fig. 1B). These results indicate that Rab6a activation of BICD2 is nucleotide-specific and demonstrates that Rab6a^{GTP} is able to activate full-length BICD2 and enhance its ability to bind to dynein and dynactin.

To further examine whether Rab6a^{GTP} can activate BICD2_{FL} and enable dynein-dynactin motility, we utilized total internal reflection microscopy (TIRF) to visualize DDB motility on microtubules. Purified dynein and dynactin from mammalian RPE-1 cell lysates were incubated with equimolar concentrations of either superfolder-GFP (sfGFP)-fused BICD2₂₅₋₄₀₀ or BICD2_{FL}, and the numbers of moving motor complexes were analyzed via kymographs (Fig. 1C). This single molecule in vitro assay revealed that BICD2₂₅₋₄₀₀ produced more processive dynein-dynactin complexes when compared to BICD2_{FL} (Fig. 1C, D, Supp. Video 1). The presence of Rab6a^{GTP} resulted in a 3-4-fold increase in the number of moving DDB complexes on microtubules, whereas Rab6a^{GDP} did not lead to any significant change over the individual DDB components alone (Fig. 1E). This result suggests that Rab6a^{GTP} is capable of alleviating the auto-inhibition of BICD2 and activating its ability to form processive DDB complexes.

Disease-related point mutations in BICD2 increase binding to dynein/dynactin and motility

Recent work has identified point mutations within the coding region of BICD2 that are present in patients diagnosed with a dominant form of spinal muscular atrophy (Peeters et al., 2013; Neveling et al., 2013; Oates et al., 2013). Using our assays, we sought to examine the effects of three BICD2_{FL} mutants identified in patients afflicted with DC-SMA/SMA-LED2 (S107L, N188T, I189F). The S107L mutation is the most frequently observed variant associated with DC-SMA (Martinez-Carrera and Wirth, 2015). We also generated a fourth mutant (F739I) that is equivalent to the conserved *Drosophila* F684I mutant that produces a bicaudal phenotype (Fig. 1A) (Wharton and Struhl, 1989; Mohler and Wieschaus, 1986). This particular mutation has been shown to have higher affinity towards dynein as compared to wild-type and was proposed to be more readily activated upon binding to cargo (Liu et al., 2013). All four of the mutations are in regions that are heavily conserved in the BICD protein family (Supp. Fig. 2A, 2B).

In a pull-down assay with Rab6a^{GTP}, the four BICD2_{FL} mutants recruited more dynein and dynactin as compared to wild-type BICD2_{FL}, with the greatest difference being observed in dynactin binding (Fig. 2A, B). An enhancement in binding also was observed with Rab6a^{GDP} or without Rab6, although the amounts of dynein-dynactin in the pull-down were much lower (Supp. Fig. 3A, B). Next, we tested the mutant constructs in the single molecule TIRF assay. In the presence of Rab6a^{GTP}, three of the BICD2_{FL} mutants (N188T, I189F, S107L) showed a statistically significant 20-30% increase in the number of motile DDB compared to wild-type BICD2_{FL} (Fig. 2C). In the presence of Rab6a^{GDP}, however, motility was lower overall and no statistical difference was observed between mutant and wild-type BICD2_{FL} (Supp. Fig 3C). With Rab6a^{GTP}, neither the velocity (Fig. 2D) nor run-length of DDB (Fig. 2E, Supp. Fig. 3D) was different between wild-type and mutant BICD2_{FL}. Thus, these results indicate the point mutations in BICD2_{FL} enhance activation by Rab6a^{GTP}, producing more motile DDB_{FL} complexes, while not altering the measured parameters of DDB_{FL} motility.

Three of the SMA mutants chosen for this study reside in the BICD2 CC1, which is the “activation domain” that joins dynactin and dynein together into a stable tripartite complex that undergoes motility (Chowdhury et al., 2015; Urnavicius et al., 2015). It is possible that these BICD2 mutations may activate motility by increasing the affinity of CC1 with dynein-dynactin and thus act independently of Rab6a and the C-terminal regulatory domain of BICD2. To test this hypothesis, we purified the mutants in the BICD2₂₅₋₄₀₀ construct, the minimal truncation that activates motility in the absence of Rab6a^{GTP}. No significant difference was observed in the number of motile DDB complexes formed by wild-type and mutant BICD2₂₅₋₄₀₀ (Fig. 2F). Wild-type and mutant BICD2₂₅₋₄₀₀ also pulled down similar amounts of dynein and dynactin (Supp. Fig. 3E). Collectively, these data suggest that the disease-associated mutations enhance the ability of Rab6a^{GTP} to relieve the autoinhibition of full-length BICD2 rather than enhance the intrinsic binding affinity of BICD2 CC1 to dynein-dynactin.

A liposome assay provides an in vitro system for cargo transport

Rab6a, like most Rab GTPases, can be prenylated by C-terminal cysteines and then targeted to exocytic and endocytic vesicles (Grigoriev et al., 2007; Utskarpen et al., 2006), where it can then bind effectors. The retrograde transport of these cargos presumably would involve membrane-bound Rab6a interacting with BICD2, which tethers dynein and dynactin. We sought to recapitulate this cargo motility in vitro using recombinant Rab6a^{GTP} or Rab6a^{GDP} covalently linked to large unilamellar vesicles (LUVs) via maleimide lipids (Fig. 3A). With Rab6a^{GTP} on the liposome, we observed the frequent binding and movement of liposomes along microtubules in the presence of dynein, dynactin, and BICD2_{FL} (Fig. 3B, C). In contrast, motility events were only rarely observed when liposomes were coated with Rab6a^{GDP} (Fig. 3B, C, Supp. Video 2). Next, we examined the BICD2_{FL} mutants in the Rab6a^{GTP} liposome motility assay. In this assay, all four of the mutants produced significant increases in the number of moving Rab6a^{GTP} liposomes compared to wild-type BICD2_{FL} (Fig. 3D). Thus, consistent with the single-molecule motility assays, the BICD2 mutants hyperactivated dynein-dynactin motility in the in vitro cargo transport assay.

Enhanced retrograde motility induced by BICD2 mutants in a cell-based assay

To examine the behavior of wild-type and mutant BICD2 in cells, we turned to a previously established inducible cargo trafficking assay (Hoogenraad et al., 2003; Kapitein et al., 2010). In this assay, FRB-BICD2 is co-expressed with FKBP fused to a peroxisome localization sequence (Fig. 4A). As shown previously, an N-terminal construct of BICD2 (BICD2₁₋₅₉₄) in the presence of rapamycin increased retrograde transport of peroxisomes and produced significant clustering of the GFP-peroxisome signal around the perinuclear region (Hoogenraad et al., 2003) (Fig. 4B). This longer construct includes part of coiled-coil 2, but still lacks the C-terminal region needed

for autoinhibition. In contrast, with cells transfected with the autoinhibited BICD2_{FL} construct, the peroxisome signal was more dispersed (Fig. 4B).

We next tested the mutant BICD2_{FL} constructs in this inducible peroxisome motility assay. To quantify the degree of peroxisome clustering due to minus-end-directed motility, we used a previously created analysis software (ICY) that calculates the fraction of the cell area containing 90% of the total peroxisome GFP signal; increased transport to the centrosome results in a more clustered signal and thus 90% of the signal occupies less area (de Chaumont et al., 2012; Mounier et al., 2012) (Fig. 4C). In the absence of rapamycin, the clustering values for the wild-type and mutants were similar (Fig. 4D), indicating that there was little non-specific motor activity trafficking the peroxisomes towards the cell center. With the addition of rapamycin to cells expressing BICD2₁₋₅₉₄, the peroxisomes moved towards the centrosome and occupied ~20% of the cell area compared with ~40% for cells expressing auto-inhibited BICD2_{FL}. The four mutants tested in the BICD2_{FL} construct, while not achieving the same degree of peroxisome clustering observed for BICD2₁₋₅₉₄, showed an increase in the compaction of the peroxisome signal compared to wild-type BICD2_{FL} (Fig. 4D). In conclusion, similar to the in vitro data, the mutant BICD2_{FL} proteins hyperactivated dynein-dynactin in a cellular context and more efficiently transported peroxisomes towards the centrosomes.

Over-expression of BICD2 mutants in hippocampal neurons decreases neurite outgrowth

Bicaudal D2 has been shown to play a role in neuronal cell migration as well as apical nuclear migration, presumably through its function as a dynein-dynactin adaptor (Jaarsma et al., 2014; Hu et al., 2013). Therefore, we next tested whether the hyperactivating BICD2_{FL} mutants affected neurite outgrowth and morphology of neurons. Rat hippocampal neurons, dissected from embryonic day 18 tissue and grown in culture, were transfected with either wild-type and

mutant mouse mCherry-BICD2_{FL} constructs along with soluble GFP to visualize the cell body and neurites (Fig. 5A). Three days later, dual mCherry and GFP positive neurons were then scored for the length of their longest process as well as the total length of all processes. Cells transfected with wild-type mCherry-BICD2_{FL} and GFP showed similar neurite lengths compared to cells transfected with GFP alone (Fig. 5B, 5C). This result is consistent with previous work showing that over-expression of wild-type BICD2 in either hippocampal or rat DRG neurons does not affect axon length or overall neurite length (Schlager et al., 2014b). However, cells transfected with the mutant BICD2_{FL} constructs for three days showed a ~40% decrease in both the length of the longest neurite as well as an overall decrease in total neurite length after three days in culture (Fig. 5B, 5C). These results demonstrate that mutations in BICD2 affect the process of neurite outgrowth of hippocampal neurons in culture.

Discussion

In this study, we developed in vitro single-molecule and liposome assays that recapitulate Rab6a^{GTP}-dependent activation of DDB motility. These assays revealed that three BICD2 mutants identified in patients afflicted with DC-SMA/SMA-LED2 (S107L, N188T, I189F) and one mutant that emerged from a *Drosophila* screen (F739I in our mammalian construct) all display a similar phenotype of eliciting more moving DDB complexes. These general findings of dynein activation were further substantiated in cells with a regulated BICD2 recruitment assay to peroxisomes. Interestingly, this effect of these human disease mutants was not evident with the Rab6a-independent, constitutively active BICD2₂₅₋₄₀₀ construct, suggesting that the mutants have minimal effect on the stability or conformation of the DDB complex. Rather, our data is most consistent with a model in which the mutants lower the energy barrier for Rab6a^{GTP} to convert the autoinhibited BICD2_{FL} into an active conformation. Future work can test this model using assays that probe the conformational states of BICD2_{FL}.

Previous cell-based models have looked for effects of BICD2 mutants that might explain the dominant phenotype of spinal muscular atrophy. One study reported that BICD2 mutants cause Golgi fragmentation, a phenotype that is often produced by interference with dynein function such as with the overexpression of the dynamitin subunit of dynactin (Burkhardt et al., 1997; Harada et al., 1998; Neveling et al., 2013). Golgi disruption is also suggested by the delocalization of Rab6a from a normal perinuclear focus to a diffusive signal in cell lines of afflicted patients (Unger et al., 2016). These studies suggest that the disease mutants may have a dominant negative effect on dynein function. While we cannot rule out dominant negative effects that cannot be measured with our assays, our data rather suggest that the mutants produce a dominant positive effect leading to enhanced dynein cargo transport. The effects are somewhat subtle (~25% increase in motile DDB complexes), but in a motor neuron with an axon

up to a meter long, such changes may be sufficient to disrupt normal cargo transport over time. To explain the SMA disease phenotype, we propose a model in which mutant BICD2 increases dynein activation and leads to an imbalance between anterograde and retrograde transport (Figure 5D). The shift towards dynein transport could produce a decrease in the delivery of cargo to the nerve terminal, which in turn could lead to a gradual decline in function of neurons with long axons. This general model is consistent with results from Schlager et al. with the BICD-related protein, BICDR-1 (M. A. Schlager, Serra-Marques, et al., 2014; M. A. Schlager et al., 2010). These investigators found that BICDR-1 expression caused the accumulation of Rab6a vesicles close to the centrosome, suggesting that BICDR-1, like our BICD2 mutants, increases dynein-driven retrograde transport. Similar to our results with BICD2 mutants, the over-expression of the wild-type BICDR-1 adapter protein resulted in a ~50% decrease in axon and total neurite length.

This model also is congruous with experimental data from transgenic animals expressing various BICD2 constructs. Mice that are BICD2 null possess a normal spinal cord and their motor neurons exhibit no evidence of abnormal retrograde transport (Jaarsma et al., 2014). While these mice die at around p30 and do experience motor function irregularities, their overall phenotype does not resemble that of SMA patients. This result suggests that the absence or inhibition of BICD2 activity cannot explain the disease etiology. In contrast, transgenic mice expressing the shorter, more active N-terminal construct of BICD2 were impaired in retrograde axonal transport and Golgi fragmentation, presumably through a dominant negative effect of activating dynein and dynactin without cargo and causing its accumulation in the cell body (Teuling et al., 2008). Curiously, however, these mice, which live up to two years, also did not develop any motor abnormalities. The phenotypic differences in mice expressing the N-terminal construct of BICD2 compared with haploid S107L, N188T, and I189F BICD2 mutations

suggests that the C-terminus of the protein that interacts with cargo is necessary for contributing to the SMA disease phenotype.

Recently, a number of disease-related mutants in the human dynein heavy chain also have been examined for their effects on motility at the single-molecule level (Hoang et al., 2017). Many of the mutants, including three mutations associated with SMA, exhibited normal DDB complex formation and velocity, but displayed a ~60-70% reduction in processivity. These data are consistent with earlier research showing that mutations (*Cra1* and *Loa*) in the heavy chain of cytoplasmic dynein that cause motor neuron disease in mouse models produce a decrease in dynein run length in vitro and an impairment of fast retrograde transport in axons (Hafezparast et al., 2003; Ori-McKenney et al., 2010). These results revealing a loss-of-function in dynein transport differ from those described for the SMA BICD2 mutants, which show no change in processivity and a gain-of-function increase in the amount of retrograde transport. Taken together, these studies on dynein and BICD2 mutations reveal multiple ways in which changes in motor activity can affect the homeostasis and function of neurons.

Acknowledgments: We thank N. Stuurman for help with microscopy, and R. McKenney for both technical help and discussions, and C. Schroeder, Y. Wang and S. Niekamp for discussions as well. This work was supported by a MIRA grant from NIGMS (NIH 1R35 GM118106).

REFERENCES

- Aitken, C.E., R.A. Marshall, and J.D. Puglisi. 2008. An oxygen scavenging system for improvement of dye stability in single-molecule fluorescence experiments. *Biophys. J.* 94:1826–1835. doi:10.1529/biophysj.107.117689.
- Allan, V.J. 2011. Cytoplasmic dynein. *Biochem. Soc. Trans.* 39:1169–78. doi:10.1042/BST0391169.
- Burkhardt, J.K., C.J. Echeverri, T. Nilsson, and R.B. Vallee. 1997. Overexpression of the dynamitin (p50) subunit of the dynactin complex disrupts dynein-dependent maintenance of membrane organelle distribution. *J. Cell Biol.* 139:469–484. doi:10.1083/jcb.139.2.469.
- de Chaumont, F., S. Dallongeville, N. Chenouard, N. Hervé, S. Pop, T. Provoost, V. Meas-Yedid, P. Pankajakshan, T. Lecomte, Y. Le Montagner, T. Lagache, A. Dufour, and J.-C. Olivo-Marin. 2012. Icy: an open bioimage informatics platform for extended reproducible research. *Nat. Methods.* 9:690–696. doi:10.1038/nmeth.2075.
- Chowdhury, S., S.A. Ketcham, T.A. Schroer, and G.C. Lander. 2015. Structural organization of the dynein – dynactin complex bound to microtubules. 1–6. doi:10.1038/nsmb.2996.
- Cianfrocco, M.A., M.E. Desantis, A.E. Leschziner, and S.L. Reck-peterson. 2015. Mechanism and Regulation of Cytoplasmic Dynein. 1–26. doi:10.1146/annurev-cellbio-100814-125438.
- Dimitriadi, M., A. Derdowski, G. Kalloo, M.S. Maginnis, B. Bliska, A. Sorkaç, K.C. Q Nguyen, S.J. Cook, G. Poulgiannis, W.J. Atwood, D.H. Hall, A.C. Hart, and E.H. by Robert Horvitz. 2016. Decreased function of survival motor neuron protein impairs endocytic pathways. doi:10.1073/pnas.1600015113.
- Edelstein, A., N. Amodaj, K. Hoover, R. Vale, and N. Stuurman. 2010. Computer control of microscopes using manager. *Curr. Protoc. Mol. Biol.* 1–17. doi:10.1002/0471142727.mb1420s92.
- Grigoriev, I., D. Splinter, N. Keijzer, P.S. Wulf, J. Demmers, T. Ohtsuka, M. Modesti, I. V Maly, F. Grosveld, C.C. Hoogenraad, and A. Akhmanova. 2007. Rab6 regulates transport and targeting of exocytotic carriers. *Dev. Cell.* 13:305–14. doi:10.1016/j.devcel.2007.06.010.
- Hafezparast, M., R. Klocke, C. Ruhrberg, A. Marquardt, A. Ahmad-Annur, S. Bowen, G. Lalli, A.S. Witherden, H. Hummerich, S. Nicholson, P.J. Morgan, R. Oozageer, J. V Priestley, S. Averill, V.R. King, S. Ball, J. Peters, T. Toda, A. Yamamoto, Y. Hiraoka, M. Augustin, D. Korthaus, S. Wattler, P. Wabnitz, C. Dickneite, S. Lampel, F. Boehme, G. Peraus, A. Popp, M. Rudelius, J. Schlegel, H. Fuchs, M. Hrabe de Angelis, G. Schiavo, D.T. Shima, A.P. Russ, G. Stumm, J.E. Martin, and E.M.C. Fisher. 2003. Mutations in dynein link motor neuron degeneration to defects in retrograde transport. *Science.* 300:808–12. doi:10.1126/science.1083129.
- Harada, A., Y. Takei, Y. Kanai, Y. Tanaka, S. Nonaka, and N. Hirokawa. 1998. Golgi vesiculation and lysosome dispersion in cells lacking cytoplasmic dynein. *J. Cell Biol.* 141:51–59. doi:10.1083/jcb.141.1.51.
- Hoang, H.T., M.A. Schlager, A.P. Carter, and S.L. Bullock. 2017. DYNC1H1 mutations associated with neurological diseases compromise processivity of dynein-dynactin-cargo adaptor complexes. *Proc. Natl. Acad. Sci.* 114:1–19. doi:10.1073/pnas.1620141114.
- Hoogenraad, C.C., P. Wulf, N. Schiefermeier, T. Stepanova, N. Galjart, J.V. Small, F. Grosveld, C.I. de Zeeuw, and A. Akhmanova. 2003. Bicaudal D induces selective dynein-mediated microtubule minus end-directed transport. *EMBO J.* 22:6004–15. doi:10.1093/emboj/cdg592.
- Hu, D.J.-K., A.D. Baffet, T. Nayak, A. Akhmanova, V. Doye, and R.B. Vallee. 2013. Dynein recruitment to nuclear pores activates apical nuclear migration and mitotic entry in brain progenitor cells. *Cell.* 154:1300–13. doi:10.1016/j.cell.2013.08.024.
- Jaarsma, D., R. van den Berg, P.S. Wulf, S. van Erp, N. Keijzer, M. a Schlager, E. de Graaff,

- C.I. De Zeeuw, R.J. Pasterkamp, A. Akhmanova, and C.C. Hoogenraad. 2014. A role for Bicaudal-D2 in radial cerebellar granule cell migration. *Nat. Commun.* 5:3411. doi:10.1038/ncomms4411.
- Kapitein, L.C., M.A. Schlager, W.A. Van Der Zwan, P.S. Wulf, N. Keijzer, and C.C. Hoogenraad. 2010. Probing intracellular motor protein activity using an inducible cargo trafficking assay. *Biophys. J.* 99:2143–2152. doi:10.1016/j.bpj.2010.07.055.
- Liu, Y., H.K. Salter, A.N. Holding, C.M. Johnson, E. Stephens, P.J. Lukavsky, J. Walshaw, and S.L. Bullock. 2013. Bicaudal-D uses a parallel, homodimeric coiled coil with heterotypic registry to coordinate recruitment of cargos to dynein. *Genes Dev.* 27:1233–46. doi:10.1101/gad.212381.112.
- Martinez-Carrera, L.A., and B. Wirth. 2015. Dominant spinal muscular atrophy is caused by mutations in BICD2, an important golgin protein. *Front. Neurosci.* 9. doi:10.3389/fnins.2015.00401.
- Matanis, T., A. Akhmanova, P. Wulf, E. Del Nery, T. Weide, T. Stepanova, N. Galjart, F. Grosveld, B. Goud, C.I. De Zeeuw, A. Barnekow, and C.C. Hoogenraad. 2002. Bicaudal-D regulates COPI-independent Golgi-ER transport by recruiting the dynein-dynactin motor complex. *Nat. Cell Biol.* 4:986–92. doi:10.1038/ncb891.
- McKenney, R.J., W. Huynh, M.E. Tanenbaum, G. Bhabha, and R.D. Vale. 2014. Activation of cytoplasmic dynein motility by dynactin-cargo adapter complexes. *Science (80-)*. 345:337–341. doi:10.1126/science.1254198.
- Mohler, J., and E.F. Wieschaus. 1986. Dominant maternal-effect mutations of *Drosophila melanogaster* causing the production of double-abdomen embryos. *Genetics.* 112:803–822.
- Mounier, J., G. Boncompain, L. Senerovic, T. Lagache, F. Chrétien, F. Perez, M. Kolbe, J.C. Olivo-Marin, P.J. Sansonetti, and N. Sauvonnet. 2012. Shigella effector IpaB-induced cholesterol relocation disrupts the golgi complex and recycling network to inhibit host cell secretion. *Cell Host Microbe.* 12:381–389. doi:10.1016/j.chom.2012.07.010.
- Neveling, K., L. a Martinez-Carrera, I. Hölker, A. Heister, A. Verrips, S.M. Hosseini-Barkoöie, C. Gilissen, S. Vermeer, M. Pennings, R. Meijer, M. te Riele, C.J.M. Frijns, O. Suchowersky, L. MacLaren, S. Rudnik-Schöneborn, R.J. Sinke, K. Zerres, R.B. Lowry, H.H. Lemmink, L. Garbes, J. a Veltman, H.J. Schelhaas, H. Scheffer, and B. Wirth. 2013. Mutations in BICD2, which encodes a golgin and important motor adaptor, cause congenital autosomal-dominant spinal muscular atrophy. *Am. J. Hum. Genet.* 92:946–54. doi:10.1016/j.ajhg.2013.04.011.
- Oates, E.C., A.M. Rossor, M. Hafezparast, M. Gonzalez, F. Speziani, D.G. MacArthur, M. Lek, E. Cottenie, M. Scoto, a R. Foley, M. Hurler, H. Houlden, L. Greensmith, M. Auer-Grumbach, T.R. Pieber, T.M. Strom, R. Schule, D.N. Herrmann, J.E. Sowden, G. Acsadi, M.P. Menezes, N.F. Clarke, S. Züchner, F. Muntoni, K.N. North, and M.M. Reilly. 2013. Mutations in BICD2 cause dominant congenital spinal muscular atrophy and hereditary spastic paraplegia. *Am. J. Hum. Genet.* 92:965–73. doi:10.1016/j.ajhg.2013.04.018.
- Ori-McKenney, K.M., J. Xu, S.P. Gross, and R.B. Vallee. 2010. A cytoplasmic dynein tail mutation impairs motor processivity. *Nat. Cell Biol.* 12:1228–1234. doi:10.1038/ncb2127.
- Peeters, K., S. Bervoets, T. Chamova, I. Litvinenko, E. De Vriendt, S. Bichev, D. Kancheva, V. Mitev, M. Kennerson, V. Timmerman, P. De Jonghe, I. Tournev, J. Macmillan, and A. Jordanova. 2015. Novel mutations in the DYNC1H1 tail domain refine the genetic and clinical spectrum of dyneinopathies. *Hum. Mutat.* 36:287–291. doi:10.1002/humu.22744.
- Peeters, K., I. Litvinenko, B. Asselbergh, L. Almeida-Souza, T. Chamova, T. Geuens, E. Ydens, M. Zimoń, J. Irobi, E. De Vriendt, V. De Winter, T. Ooms, V. Timmerman, I. Tournev, and A. Jordanova. 2013. Molecular Defects in the Motor Adaptor BICD2 Cause Proximal Spinal Muscular Atrophy with Autosomal-Dominant Inheritance. *Am. J. Hum. Genet.* 92:955–964. doi:10.1016/j.ajhg.2013.04.013.

- Reck-Peterson, S.L., A. Yildiz, A.P. Carter, A. Gennerich, N. Zhang, and R.D. Vale. 2006. Single-Molecule Analysis of Dynein Processivity and Stepping Behavior. *Cell*. 126:335–348. doi:10.1016/j.cell.2006.05.046.
- Schlager, M.A., H.T. Hoang, L. Urnavicius, S.L. Bullock, and A.P. Carter. 2014a. In vitro reconstitution of a highly processive recombinant human dynein complex. *EMBO J*. 33:1855–68. doi:10.15252/embj.201488792.
- Schlager, M.A., A. Serra-Marques, I. Grigoriev, L.F. Gummy, M. Esteves da Silva, P.S. Wulf, A. Akhmanova, and C.C. Hoogenraad. 2014b. Bicaudal D Family Adaptor Proteins Control the Velocity of Dynein-Based Movements. *Cell Rep*. 1–9. doi:10.1016/j.celrep.2014.07.052.
- Schlager, M. a, L.C. Kapitein, I. Grigoriev, G.M. Burzynski, P.S. Wulf, N. Keijzer, E. de Graaff, M. Fukuda, I.T. Shepherd, A. Akhmanova, and C.C. Hoogenraad. 2010. Pericentrosomal targeting of Rab6 secretory vesicles by Bicaudal-D-related protein 1 (BICDR-1) regulates neuritogenesis. *EMBO J*. 29:1637–51. doi:10.1038/emboj.2010.51.
- Schroeder, C.M., and R.D. Vale. 2016. Assembly and activation of dynein-dynactin by the cargo adaptor protein Hook3. *J. Cell Biol*. 214:309–318. doi:10.1083/jcb.201604002.
- Splinter, D., D.S. Razafsky, M. a Schlager, A. Serra-Marques, I. Grigoriev, J. Demmers, N. Keijzer, K. Jiang, I. Poser, A. a Hyman, C.C. Hoogenraad, S.J. King, and A. Akhmanova. 2012. BICD2, dynactin, and LIS1 cooperate in regulating dynein recruitment to cellular structures. *Mol. Biol. Cell*. 23:4226–41. doi:10.1091/mbc.E12-03-0210.
- Teuling, E., V. van Dis, P.S. Wulf, E.D. Haasdijk, A. Akhmanova, C.C. Hoogenraad, and D. Jaarsma. 2008. A novel mouse model with impaired dynein/dynactin function develops amyotrophic lateral sclerosis (ALS)-like features in motor neurons and improves lifespan in SOD1-ALS mice. *Hum. Mol. Genet*. 17:2849–2862. doi:10.1093/hmg/ddn182.
- Unger, A., G. Dekomien, A. Güttsches, R. Kley, M. Tegenthoff, A. Ferbert, J. Weis, W.A. Linke, L. Martinez-carrera, and M. Storbeck. 2016. Expanding the phenotype of BICD2 mutations toward skeletal muscle involvement. 1–10.
- Urnavicius, L., K. Zhang, A.G. Diamant, C. Motz, M.A. Schlager, M. Yu, N.A. Patel, C. V. Robinson, and A.P. Carter. 2015. The structure of the dynactin complex and its interaction with dynein. *Science (80-.)*. 6:467–477. doi:10.7897/2230-8407.06796.
- Utskarpen, A., H.H. Slagsvold, T.-G. Iversen, S. Walchli, and K. Sandvig. 2006. Transport of ricin from endosomes to the golgi apparatus is regulated by Rab6A and Rab6A???. *Traffic*. 7:663–672. doi:10.1111/j.1600-0854.2006.00418.x.
- Wharton, R.P., and G. Struhl. 1989. Structure of the *Drosophila* BicaudalD protein and its role in localizing the posterior determinant nanos. *Cell*. 59:881–892. doi:10.1016/0092-8674(89)90611-9.

Figure Legends

Figure 1: BICD2_{FL} activation by Rab6a^{GTP}.

(A) Domain architecture of mammalian Bicaudal D2 (BICD2). The protein is comprised of three stretches of coiled-coil regions, CC1-CC3, with select binding partners indicated. N188T, I189F, and S107L highlight some of the mutations associated with human SMA-LED, and F739I is the analogous mutation to the classical Drosophila mutation, F684I. Amino acids 400 and 594 indicate the end of constructs used in this study. (B) Porcine brain lysate pull-down using Strep-tagged full-length BICD2 as bait bound to Strep-tactin resin. Increasing amounts of recombinant Rab6a^{GTP} (left) or Rab6a^{GDP} (right) was added to the lysate, and the amount of endogenous dynein (dynein intermediate chain (DIC) and dynactin (p150 subunit) pulled bound was analyzed by immunoblot. (C) Sample kymographs of single molecule DDB (a.a. 25-400 or full-length (FL) BICD2) motility on microtubules. Fluorescence is from the N-terminal sfGFP tag on BICD2. (D) Quantification of the number of moving motors per micron of microtubule; mean and SD from n = 3 independent experiments (each experiment measuring a minimum of 30 microtubules). (E) Quantification of number of moving motors per micron of microtubule of full-length BICD2_{FL} with either Rab6a^{GDP} or Rab6a^{GTP} added; mean and SEM from n = 3 independent experiments (each experiment measuring a minimum of 30 microtubules).

Figure 2: BICD2_{FL} mutants show increased binding to dynein/dynactin and single molecule motility in vitro.

(A) Porcine brain lysate pull-down using Strep-tagged BICD2_{FL} as bait on Strep-tactin resin. Rab6a^{GTP} or Rab6a^{GDP} was added to the lysate at a concentration of 1 μ M. The amount of endogenous dynein (dynein intermediate chain (DIC) and dynactin (p150 subunit) pulled bound was analyzed by immunoblot. The amount of BICD2 on beads was visualized using Coomassie stain. (B) The ratio of dynein or dynactin band intensity for mutants compared to wild-type

BICD2 for the scenario in which Rab6a^{GTP} is added; mean and SEM from n = 3 independent experiments. Quantitation for the other conditions is found in Supp. Fig 3 A, B. **(C)** Dynein and dynactin (purified from RPE-1 cells; see Methods) were incubated with BICD2 and flowed into a motility chamber. The number of moving DDB motors, as visualized by sfGFP fluorescence on BICD2, was quantified per min per micron length of microtubules in the assay; mean and SEM from n = 3 independent experiments. (each experiment measuring a minimum of 30 microtubules) [$*P \leq 0.05$]. **(D)** Velocities of the moving motors from part C is shown; mean and SEM from n = 3 independent protein preparations and experiments (each experiment measuring a minimum of 100 DDB complexes). **(E)** The run lengths of WT and mutant DDB_{FL}; mean and SEM from n = 3 independent experiments (each experiment measuring a minimum of 130 DDB complexes). For processivity measurements, the NaCl concentration was increased from 50 to 65 mM to reduce the run length so that it could be more reliably measured (see Methods). **(F)** Purified dynein and dynactin were incubated with truncated BICD2₂₅₋₄₀₀ (WT and mutant) and flowed into a motility chamber. The number of moving DDB complexes, as visualized by SNAP-TMR fluorescence on BICD2, was quantified per min per micron of microtubule; mean and SEM from n = 3 independent protein preparations and experiments (each experiment measuring a minimum of 30 microtubules).

Figure 3: A motility assay using liposomes recapitulates single molecule data

(A) A schematic of the liposome motility assay. Rab6a was conjugated to maleimide lipids incorporated into 200 nm-sized liposomes and incubated in solution with DDB. Liposomes were labeled with 0.1% rhodamine-PE. **(B)** Representative kymographs of Rab6a^{GDP} vs Rab6a^{GTP} liposomes moving along microtubule in the presence of DDB_{FL}. Horizontal dash lines represent liposomes transiently entering the field of focus. **(C)** Quantification of number of motile Rab6a^{GDP} or Rab6a^{GTP} liposomes when incubated with DDB_{FL}; mean and SD from n = 3 independent experiments (each experiment measuring a minimum of 30 microtubules. Runs for

Rab6a^{GDP} occurred very infrequently). **(D)** Quantification of the number of motile Rab6a^{GTP} liposomes moving on microtubules when **incubated** with DDB_{FL} (wild-type (WT) vs mutant); mean and SEM from n = 3 independent experiments (each experiment measuring a minimum of 30 microtubules) [***P ≤ 0.001, **P ≤ 0.01] .

Figure 4: In vivo dynein-dynactin motility induced by wild-type and mutant BICD2.

(A) Schematic of the in vivo peroxisome motility assay. U2OS cells were co-transfected with a plasmid expressing GFP-FRB with a PEX3 localization sequence, targeting the protein to peroxisomes, and a BICD2-mCherry-FKBP construct. After addition of rapamycin, BICD2-mCherry-FKBP is recruited to peroxisomes. If in an active state, the BICD2 recruits dynein-dynactin which transport the peroxisome along microtubules towards their minus ends, which are clustered at the centrosome. **(B)** Representative epi-fluorescence images of the assay for both BICD2₁₋₅₉₄ and BICD2_{FL}. Peroxisomes are shown in green, the white signal represents the far-red cell membrane marker, and blue is DAPI. In the absence of rapamycin, peroxisomes decorated with GFP-FRB are distributed throughout the cytoplasm (columns 1 and 3). 1 hr after rapamycin addition, peroxisomes in cells expressing BICD2₁₋₅₉₄ are heavily clustered at the cell center (column 2), while those expressing BICD2_{FL} exhibit less clustering (columns 4). Scale Bar: 10 μM. **(C)** Example image of an analyzed cell. The white outline depicts the cell boundary; the inner green line indicates the area that contains 90% of fluorescence (see Methods). Scale Bar: 10 μM. **(D)** and **(E)** Quantification of the cell clustering data. The percentage of the cell area in which 90% of total fluorescence was contained is used as a measure for the degree of clustering (see Methods). Lower values reflect a higher degree of clustering; mean and SD from n = 3 independent experiments (each experiment measuring a minimum of 25 cells for each construct) [*P ≤ 0.05].

Figure 5: Over-expression of BICD2 mutants in rat hippocampal neurons results in a decrease in neurite length.

(A) Representative images of hippocampal neurons over-expressing mCherry-BICD2_{FL} (wild-type and mutants) or an empty plasmid control; neurons were also co-transfected with soluble GFP in order to mark the neurites. Scale Bar: 10 μ M. (B) Axon length after 3 days of over-expression of BICD2_{FL} constructs; mean and SD from n = 3 independent experiment (each experiment measuring 15-20 neurons for each construct) [$*P \leq 0.05$]. (C) Total neurite length after 3 days of over-expression of BICD2_{FL} constructs; mean and SD from n = 3 independent experiment (each experiment measuring 15-20 neurons for each construct) [$**P \leq 0.01$]. (D) Model of how a gain-of-function in dynein-based motility from BICD2 mutants might cause a misbalance of axonal transport and lead to SMA. See Discussion for more details.

Materials and Methods

DNA constructs

The cDNAs for mouse BICD2 (accession #AJ250106.1) and mouse Rab6a (accession #BC019118.1) were obtained from the Thermo Scientific MGC collection. BICD2 N-terminal constructs were cloned into a pet28a vector containing an N-terminal 6xHis-strepII-sfGFP tag. Full-length BICD2 WT and mutant constructs were cloned into a pFastbac vector containing either an N-terminal StrepII-sfGFP or StrepII-SNAPf tag followed by a C-terminal 6xHis tag for tandem purification. Rab6a was cloned into a pGEX vector containing an N-terminal GST tag followed by a PreScission protease cleavage site. The Rab6a constructs span the GTPase domain of Rab6a (a.a. 8-195), followed by a short linker and either a KCK motif for maleimide labeling purposes (liposome experiment), or a His10-tag. Point mutations for both the BICD2 constructs and the Rab6a GDP/GTP (Q72L and T27N, respectively) constructs were created by the protocol of Phusion, Inc.

For the cell-based peroxisome assay, the sequence spanning amino acids 1-42 of human PEX3 was synthesized via a gBlock (IDT), and was cloned into the N-terminal of a modified eGFP vector, followed by a C-terminal FRB sequence. BICD2 constructs for this assay were cloned into a pHR vector containing an N-terminal mCherry sequence and C-terminal FKBPf36v sequence. For neuron expression, BICD2 was cloned into an N-terminal pmCherry vector.

Protein Purification

BICD2 N-terminal and Rab6a constructs were transformed into the *Escherichia coli* strain BL21 RIPL from Agilent. Cells were grown in LB at 37°C until growth reached ~0.6 OD₂₈₀. The temperature was then lowered to 18°C and cells were induced over-night with 0.5 mM IPTG.

Bacterial pellets were resuspended in either strep lysis buffer (30 mM HEPES, pH 7.4, 300 mM NaCl, 2 mM MgCl₂, 5% glycerol, 5 mM DTT, 1 mM PMSF) for BICD2 or PBS containing 5% glycerol, 5 mM DTT, and 1 mM PMSF for Rab6a. Cells were lysed using an Emulsiflex press (Avestin) and clarified at 40,000g for 60 min. Lysates were bound to either Strep-tactin Superflow Plus resin (QIAGEN) or GST Sepharose 4B (GE Lifesciences). Beads were then washed extensively and the bound protein was eluted with 3 mM desthiobiotin in lysis buffer (BICD2) or via overnight cleavage with PreScission (Rab6a).

BICD2 full-length constructs were purified from SF9 cells and purified using tandem purification. Bacmids isolated from DH10Bac cells were transfected into SF9 cells. P2 virus was used to infect SF9 cells grown in shaker flasks to a density of 2x10⁶ cells/ml. After ~60 hr of infection, cells were harvested, pelleted, and resuspended in NiNTA lysis buffer (30 mM HEPES pH 7.4, 300 mM NaCl, 5% glycerol, 20 mM imidazole, 1 mM PMSF, 5 mM βME) and lysed using an Emulsiflex. The lysate was clarified at 40,000g for 1 hr and bound to NiNTA resin from Qiagen. After extensively washing with lysis buffer, cells were eluted with lysis buffer containing 500 mM imidazole. The eluted material was then diluted to lower the imidazole concentration to 100 mM, and bound to Streptactin beads as described above. After elution, proteins were concentrated and injected onto either a Superose 6 10/300GL column (BICD2 constructs) or a S200 10/300GL column (Rab6a) from GE healthcare. Gel filtration buffer was comprised of: 30mM HEPES pH 7.4, 150mM NaCl, 10% glycerol, 2mM TCEP. Peak fractions were pooled and concentrated and then flash frozen. For SNAP-fusion constructs, purified proteins were bound to Streptactin beads and incubated at a 2:1 ratio of SNAP-TMR Star:Protein on ice for 1 hour. Beads were briefly washed in the gel filtration buffer and the protein was eluted with 3mM of desthiobiotin in gel filtration buffer.

Dynein and dynactin were prepared from RPE-1 cells, as previous described (Schroeder and Vale, 2016).

Porcine Brain Pull-downs

Pull-downs were performed as previously described (McKenney et al., 2014). Briefly, clarified porcine brain lysate in Buffer A (30 mM HEPES pH 7.4, 50 mM potassium acetate, 2 mM magnesium acetate, 1 mM EGTA, 10% glycerol) was added to Streptactin Sepharose beads (GE Healthcare) along with 100 nM of the BICD2 construct to be tested. To this mixture, 0.1% of NP-40, 1 mM PMSF, and 5 mM DTT were added and the mixture was incubated at 4°C for 1 hr. The beads were then pelleted and washed 4 times with Buffer A containing 0.1% NP-40 and 5 mM DTT. The proteins were then eluted using SDS loading buffer and resolved on an acrylamide gel (Invitrogen). For experiments where Rab6a was supplemented, the appropriate amount of recombinant Rab6a protein was added prior to the 4°C incubation step and processed in the same fashion.

Immunoblot Analysis

The SDS-PAGE gel was transferred onto a nitrocellulose membrane using the iBlot system from Invitrogen. Western blotting was performed using TBS buffer with 0.1% Tween-20 (TBS-T). Membranes were blot for 1 hr at room temperature with 5% milk in TBS-T, followed by a 1 hr primary antibody incubation. Antibodies used are as follows: mouse anti-p150 (clone 12, 1:250; BD), mouse anti-dynein intermediate chain (clone 74.1, 1:1000; EMD Millipore), mouse anti-6xHis (1:1000, Roche), mouse anti-Rab6a (ab55660, 1:500, Abcam). Membranes were washed 3x with TBS-T and then incubated with a secondary antibody for 1 hr at r.t. Secondary antibodies were: anti-mouse-800 or anti-rabbit-680 (1:10,000; Molecular Probes). Membranes were washed 3x with TBS-T and then imaged using an Odyssey Clx Infrared Imaging System

(LI-COR Biosciences). Quantification of band intensity was performed using ImageJ's (NIH) gel analysis feature.

Liposome preparation and Rab6a labeling

Liposomes were prepared from a mixture of lipids dissolved in chloroform at (82.4% POPC, 15% POPS, 2.5% 18:1 PE MCC, 0.1% rhodamine PE (Avanti)). After mixing, they were dried under a constant stream of argon and then desiccated in vacuum overnight. The lipid film was then resuspended with Buffer A without glycerol and passed 25X through an extruder containing a 200 nm pore size polycarbonate filter. A 3:1 ratio of Rab6a to maleimide lipid was then mixed together and incubated overnight. The next day, DTT was added to a final concentration of 10 mM to quench the reaction, and the liposomes were pelleted at 160,000g for 20 minutes to remove unlabeled Rab6a. The pellet was then washed and resuspended with Buffer A.

Single-molecule and liposome imaging

Preparation of microtubules. Microtubules were prepared as previously described (McKenney et al., 2014). Unlabeled tubulin was mixed with biotinylated tubulin and Alexa-640 labeled tubulin at a ratio of ~10:2:2 in BRB80 (80 mM PIPES, pH 6.8, 1 mM EGTA, 1 mM MgCl₂). 5 mM GTP was added and the mixture was incubated in a 37°C water bath for 10 min before adding. 20 μM of Taxol and incubated for an additional 50 min at 37°C. Microtubules were spun over a 25% sucrose cushion at 160,000 g for 10 min in a tabletop centrifuge prior to use.

Preparation of DDB complexes and imaging. DDB complexes were formed in a 30 μL reaction volume containing ~20 nM of recombinant BICD2, ~0.15 mg/ml of dynein/dynactin, and Buffer A along with 0.1 mg/ml Biotin-BSA, 0.5% pluronic acid F-127, and 0.2 mg/ml κ-casein (Buffer B). The proteins were mixed and incubate on ice for 20 min prior to use. In experiments where

Rab6a was also included, the respective construct was added to a final concentration of 1 μ M. Flow chambers with attached microtubules were performed as described (Schroeder and Vale, 2016). A 1:4 or 1:5 dilution of the DDB complex in Buffer B was then added in presence of 1 mM ATP and the Trolox/PCA/PCD oxygen scavenging system (Aitken et al., 2008). Because the run-lengths using Buffer B tended to span the entire lengths of our microtubules, we added 15 mM of KCl to Buffer B (termed Buffer C) for measurement of processivity. The increased amount of salt in Buffer C reduced the run length for DDB (\sim 4 μ m) so that it could be measured more accurately on microtubules (average length of \sim 16 μ m used in these measurements). For liposome assays, the same components as in the DDB mixture above was mixed in a tube, along with either Rab6a^{GTP} or Rab6a^{GDP} liposomes. The liposomes were diluted to a final concentration of \sim 2.5 μ M total lipid. After incubation, the solution was flowed in undiluted into an imaging chamber after addition of 1 mM ATP and Trolox/PCA/PCD.

Total internal reflection fluorescence images were acquired on a Nikon Eclipse TE200-E microscope equipped with an Andor iXon EM CCD camera, a 100x 1.49 NA objective, and MicroManager software (Edelstein et al., 2010). Exposures of 100 or 200 ms with a frame interval of 1 per sec for 300 sec was typically utilized for the acquisition.

Peroxisome Assay in U2OS cells

U2OS cells from ATCC were cultured in DMEM medium containing 10% FCS and 1x penicillin/streptomycin/glutamine. Cells were seeded in glass-bottom 96 well plates and were at \sim 40% confluence on the day of transfection. Cells were transfected with TransIT Lt1 as per the manufacturer's protocol with a combination of the PEX-eGFP-FRB and mCherry-BICD2-FKBP plasmids and incubated overnight. The next day, 1 μ M of rapamycin or DMSO were added to cells and allowed to incubate at 37°C for 1 hr. 10 min before the end of this incubation, Cell

Mask Far Red (ThermoFisher) was added (0.5x of the manufacturer's solution) to stain the plasma membrane. Cells were then washed with PBS and fixed with 4% paraformaldehyde (PFA) at room temperature followed by extensive washing with PBS. Cells were imaged using an inverted Nikon Eclipse Ti microscope with a camera using a 40x air objective, Andor Xyla camera, and Micro-Manager software (Edelstein et al., 2010).

Primary hippocampal neuron cultures and transfection

Primary hippocampal neuron cultures were prepared from tissue from embryonic day 18 (E18) rat brains which were shipped over-night on ice from Brainbits LLC. Cells were prepared according to provider's instructions. Briefly, the tissue was incubated with a 2 mg/ml solution of papain in Hibernate E without calcium (Brainbits) for 10 min at 30°C. The tissue was then triturated using a fire polished Pasteur pipette for 1 min and then large tissue pieces were allowed to settle for 1 min. The supernatant was collected and centrifuged at 200xg for 1 min to collect cells. After removal of most of the supernatant, the pellet was resuspended with 1 ml of NbActiv1 and the cells were counted after staining with Trypan Blue (1:5 dilution). ~50,000 cells were seeded onto poly-d lysine/laminin coated round coverslips (Corning BioCoat) placed into wells of a 24-well plate.

One day after plating, neurons were transfected using Lipofectamine 2000 (Invitrogen). Each transfection reaction contained 1 µg of total plasmid DNA along with 4 µL of Lipofectamine reagent incubated together for 20 min at r.t. Media from the neurons was then removed and saved and fresh NbActiv was added to the wells along with the transfection mixture. After 2.5 hr at 37°C in 5% CO₂, the neurons were washed with NbActiv and the original conditioned media was added back. Cells were fixed 3 days after transfection using 4% PFA for 20 min at room temperature. After washing, the coverslips were mounted onto slides using Vectashield (Vector

Labs). Neurons were imaged using a Zeiss Axiovert 200M microscope using a 20x air objective, Hamamatsu C4742-98 CCD camera, and Micro-manager software (Edelstein et al., 2010).

Image Analysis and Quantification

Analysis of DDB motility and run length. Kymographs were created from the single molecule or liposome movies using ImageJ. The number of runs per micron of MT per unit of time was obtained from these kymographs, with each run being scored if it was $>1 \mu\text{m}$ in length. The cumulative frequency was used for analysis of run lengths, as previously described (McKenney et al., 2014). The 1-cumulative frequency distribution was fitted with a one-phase exponential decay.

Analysis of peroxisome clustering. The images acquired from fixed U2OS cells were processed and analyzed using the Compaction Profiler plugin previously developed for the ICY software (Mounier et al., 2012). Briefly, the fluorescent signal from the GFP channel corresponding to peroxisomes were detected after masking the shape of cell via the CellMask channel and quantified using the Spot Detector plugin in ICY. The detected fluorescence data was then passed along to the Compaction Profiler plugin, which then calculated the area of an ROI inside the cell that represents 90% of the total fluorescence signal. A higher degree of clustering results in a smaller calculated area, whereas a more diffusive signal yields a larger area.

Analysis of primary hippocampal neurons. Neurite lengths were measured using the soluble GFP signal from the transfected plasmid. The Imagej plugin NeuronJ was utilized to trace all neurites including branches from individual neurite. The longest neurite from a cell was also identified and measured.

Supplemental Figure Legends

Fig. S1. BICD2₂₅₋₄₀₀ recruits more dynein as compared to full-length. (A) A comparison of the amounts of dynein and dynactin pulled down from porcine brain lysate between BICD2₂₅₋₄₀₀ and BICD2_{FL}. (B) Quantification of the pull-down; mean and from n = 3 independent experiments. (C) Top - The supernatant fraction of the pull-downs from Figure 1B, showing that similar amounts of dynein and dynactin were present in the brain lysate across the conditions tested. Bottom – the immunoblot shows that Rab6a^{GTP} but not Rab6a^{GDP} binds to the BICD2 beads.

Fig. S2. Point mutations are conserved in BICD2. (A) A sequence alignment of Drosophila, human, and mouse BICD2 with the mutations used in this study highlighted. (B) Gels of the purified full-length BICD2 proteins are shown.

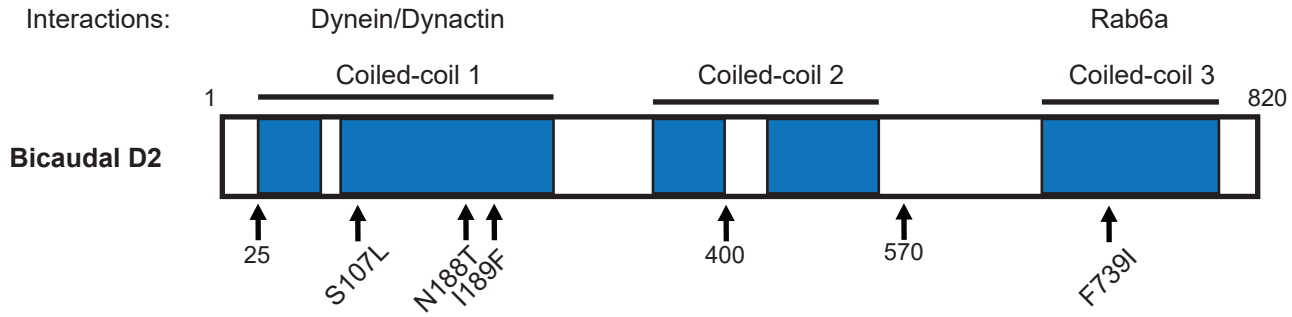
Fig. S3. N-terminal mutant constructs of BICD2 are comparable to WT. (A) and (B) show the quantification of the western blots for no-Rab6a and Rab6a^{GDP} pull-downs from Figure 2; mean and SD from n = 3 independent experiments. (C) The motility assay for DDB + Rab6a^{GDP} is also shown; mean and SD from n = 3 independent experiments. (D) Processivity data in the form of a 1-cumulative frequency histogram for one replicate, comparing different full-length BICD2 constructs. (E) A comparison of BICD2₂₅₋₄₀₀ for WT and appropriate mutant constructs in the porcine brain lysate pull-down assay. Shown are the western blots of the pellet fractions for p150 and DIC and a Coomassie staining for BICD2.

Supplemental Movie Legends:

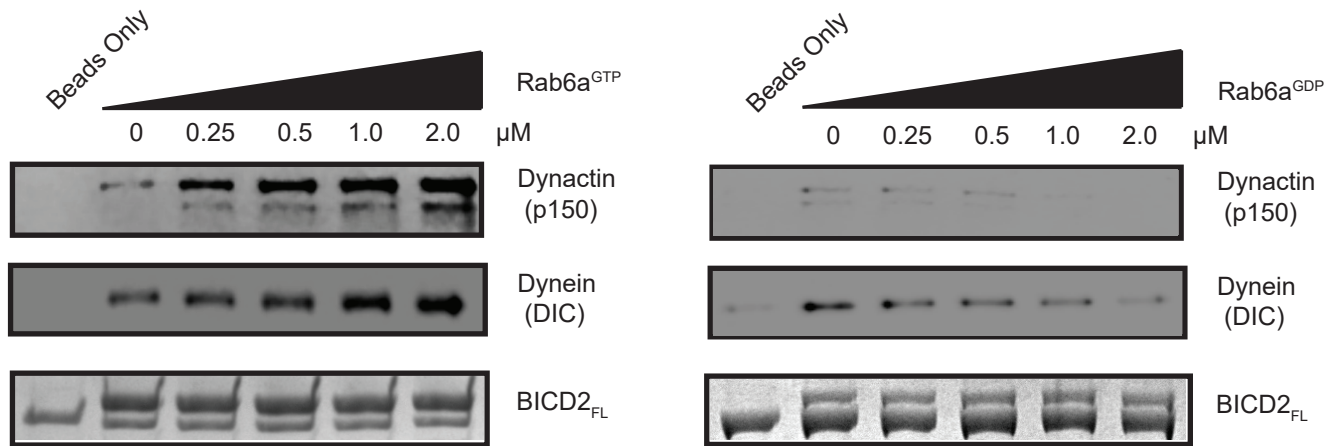
Video S1. Comparison of BICD2₂₅₋₄₀₀ vs BICD2_{FL} DDB. Movie shows motility of either BICD2₂₅₋₄₀₀ (left) or BICD2_{FL} (right) DDB complexes (green) on microtubules (blue). Scale bar is 2 μ M. See Figure 1C for details.

Video S2. Comparison of Rab6a^{GDP} and Rab6a^{GTP} liposome motility. Movie shows a comparison of Rab6aGDP (left) vs Rab6aGTP (right) liposomes (red) when incubated together with DDB_{FL}. Microtubules are shown in blue. Scale bar is 2 μ M.

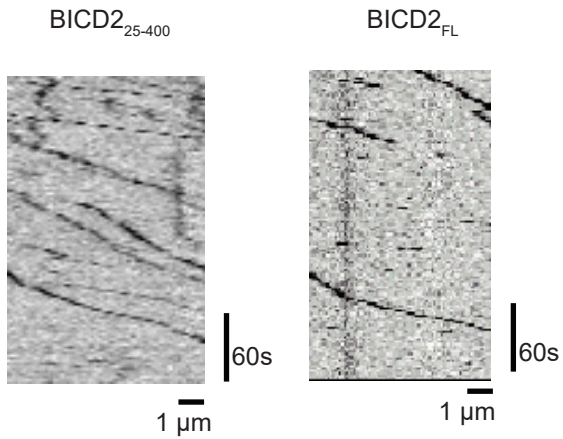
A.



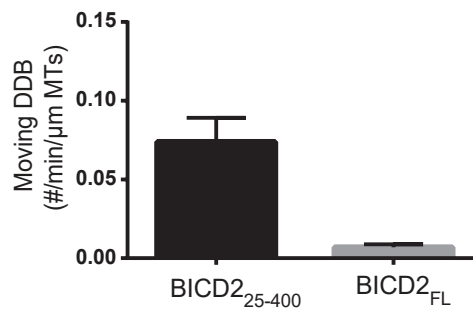
B.



C.



D.



E.

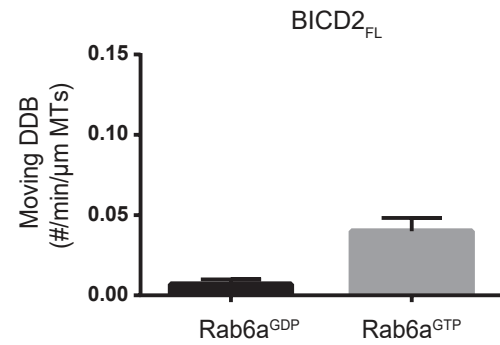
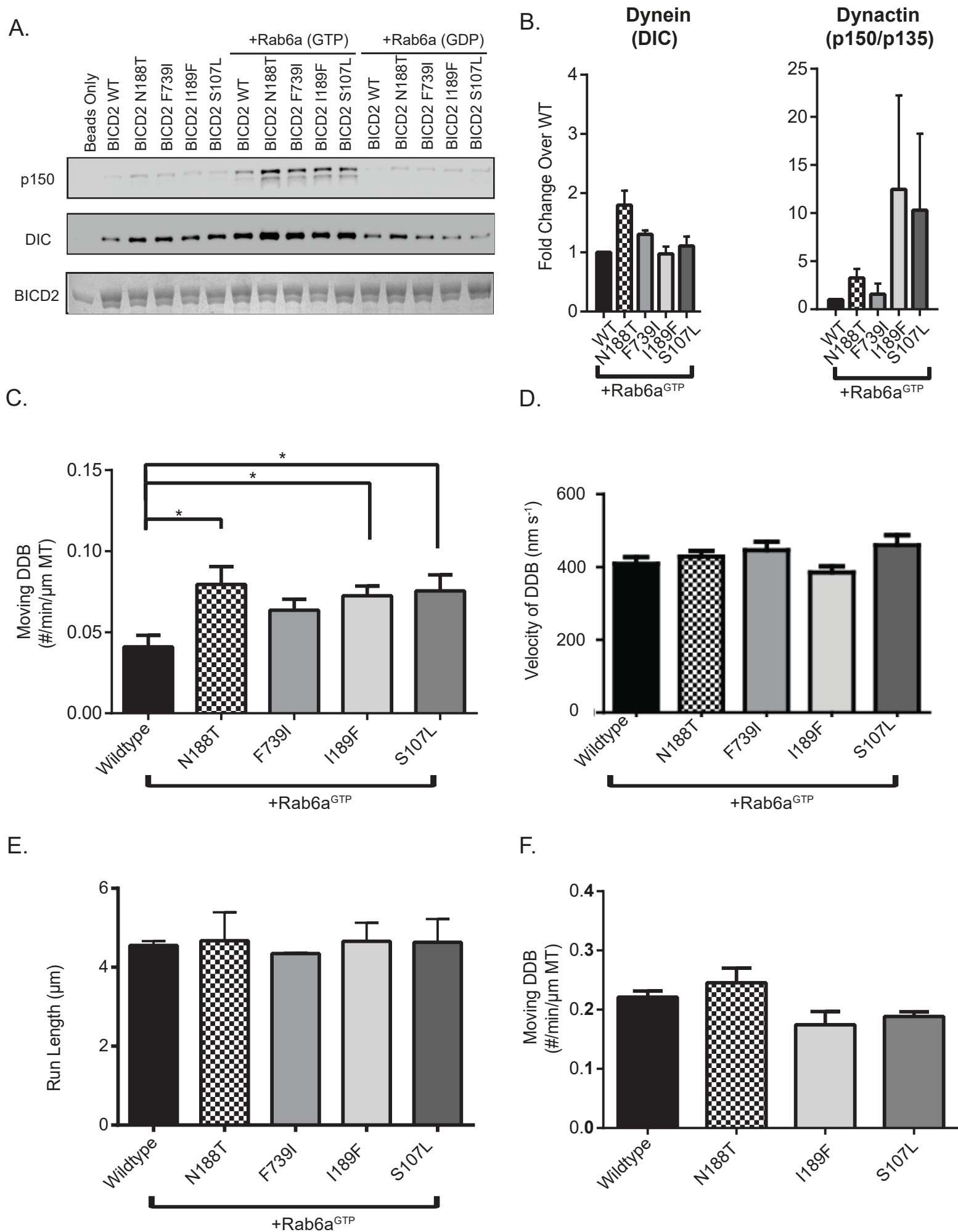
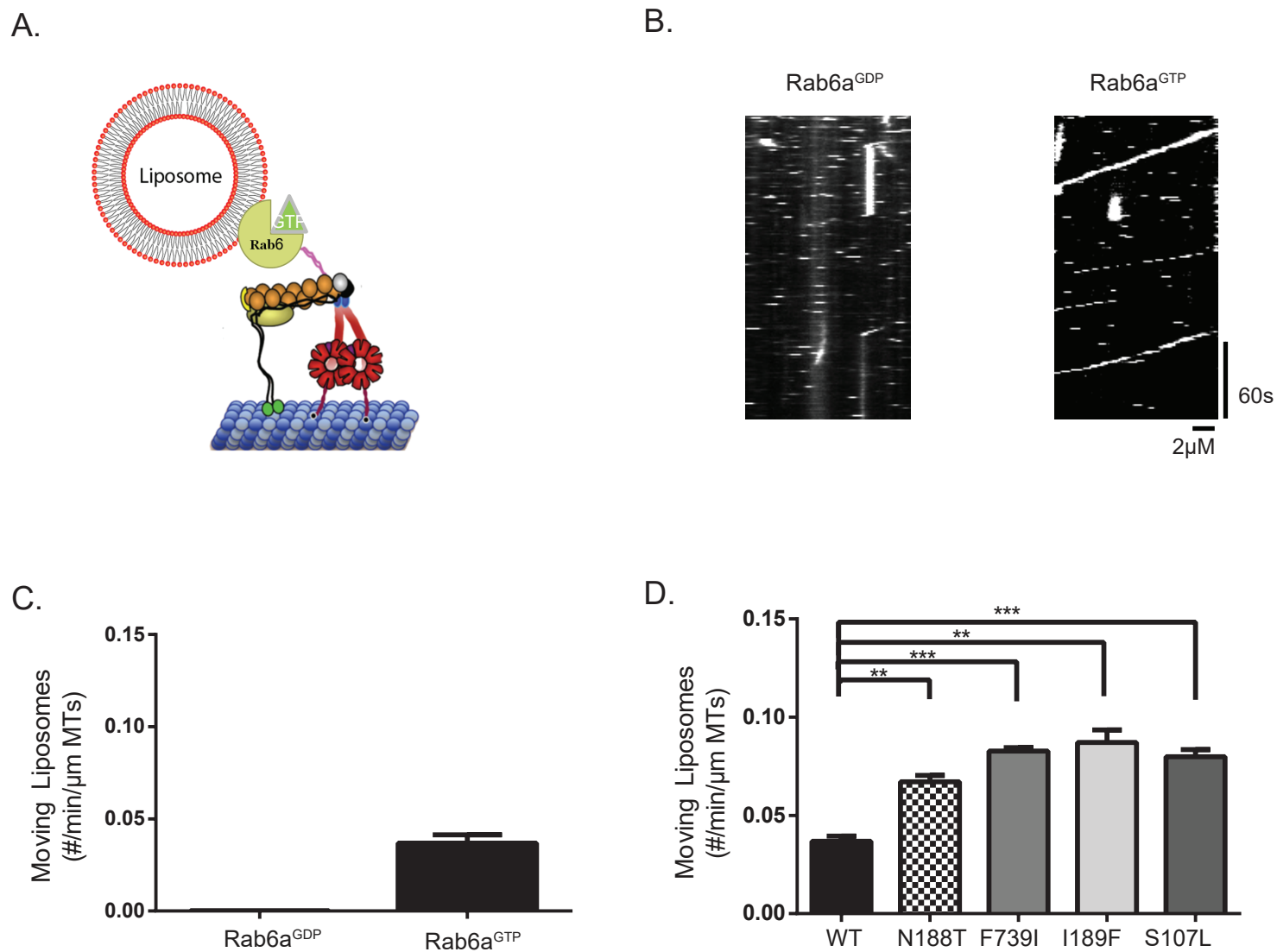
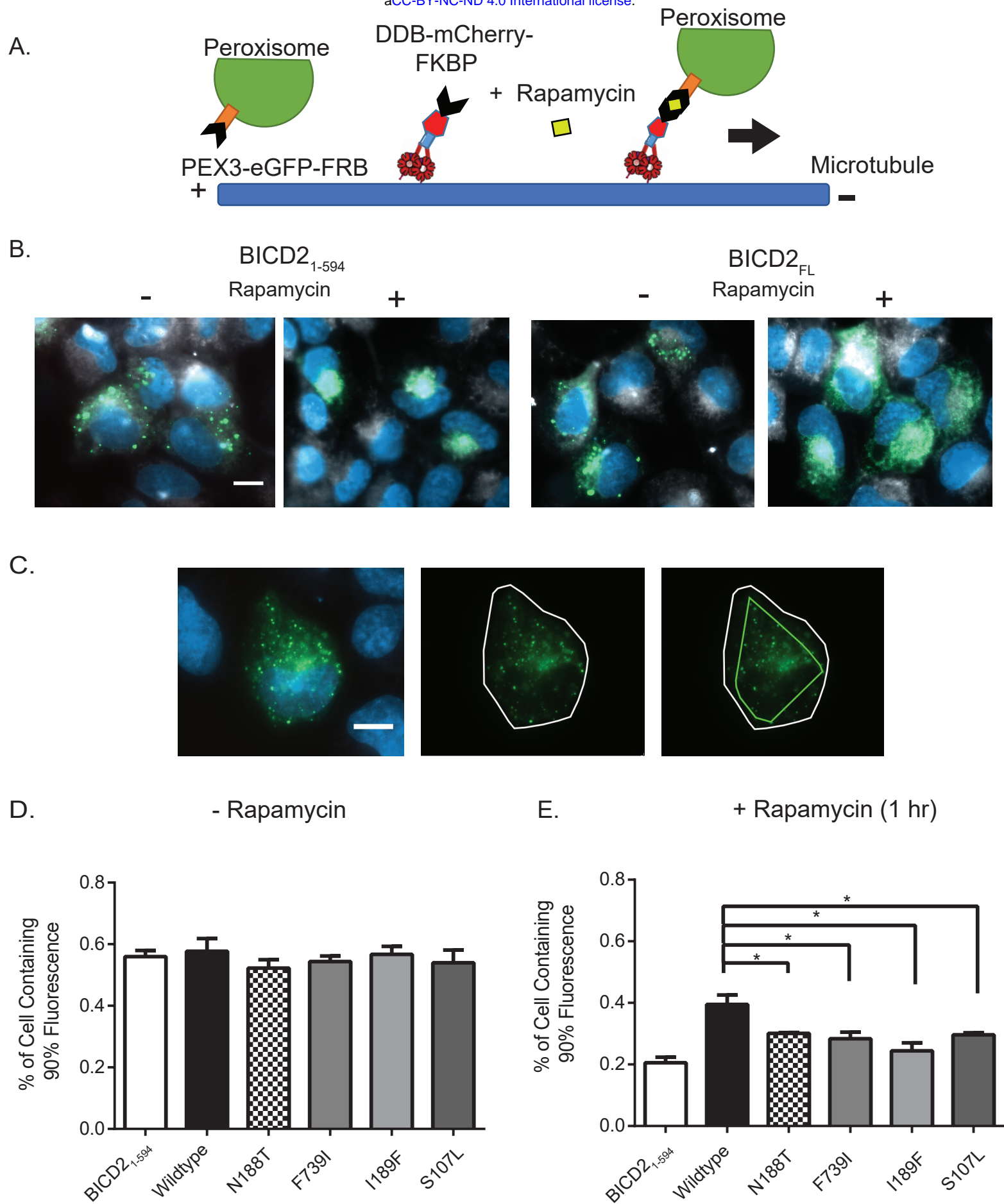


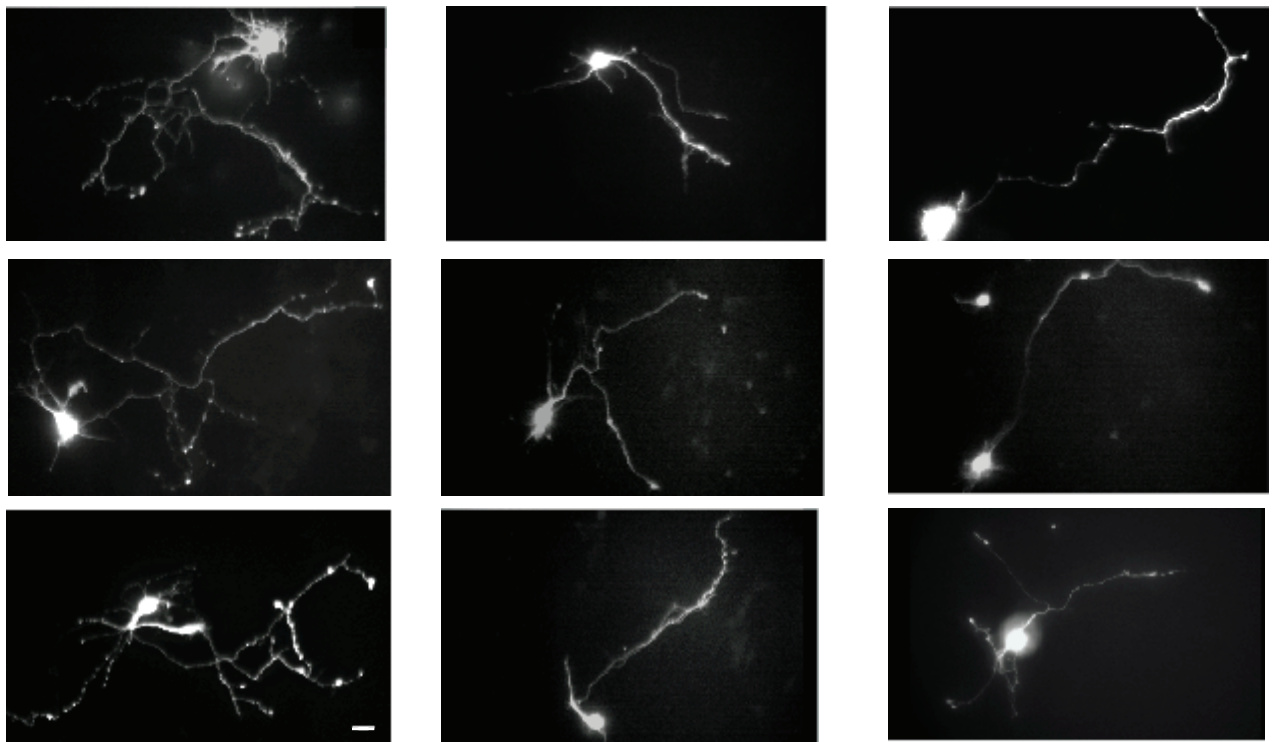
Figure 2. BICD2 mutants show increased binding to dynein and dynactin.







A.



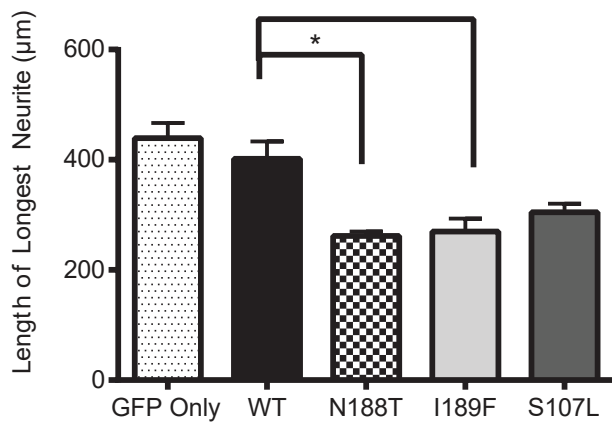
Wildtype

N188T

I189F

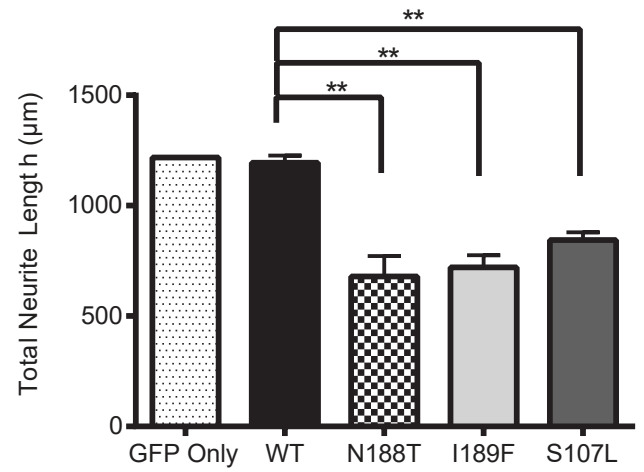
B.

Longest Neurite



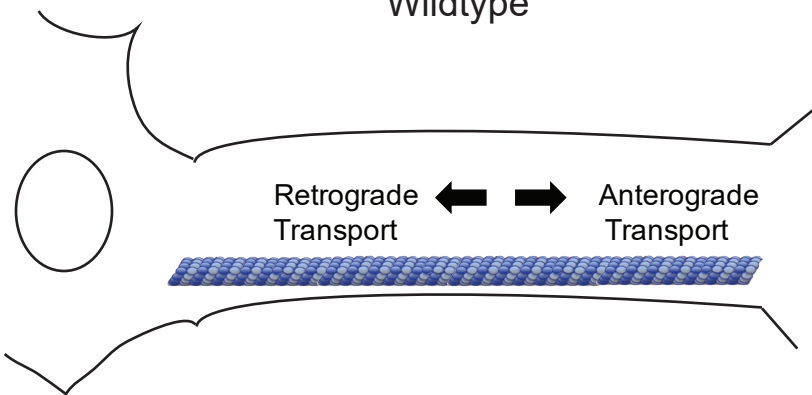
C.

Total Length of All Neurites

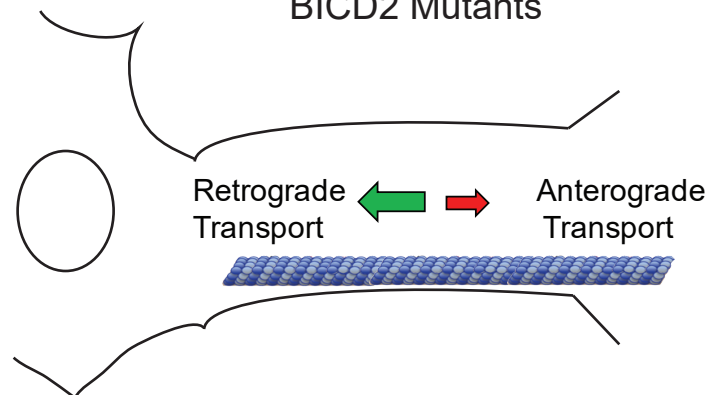


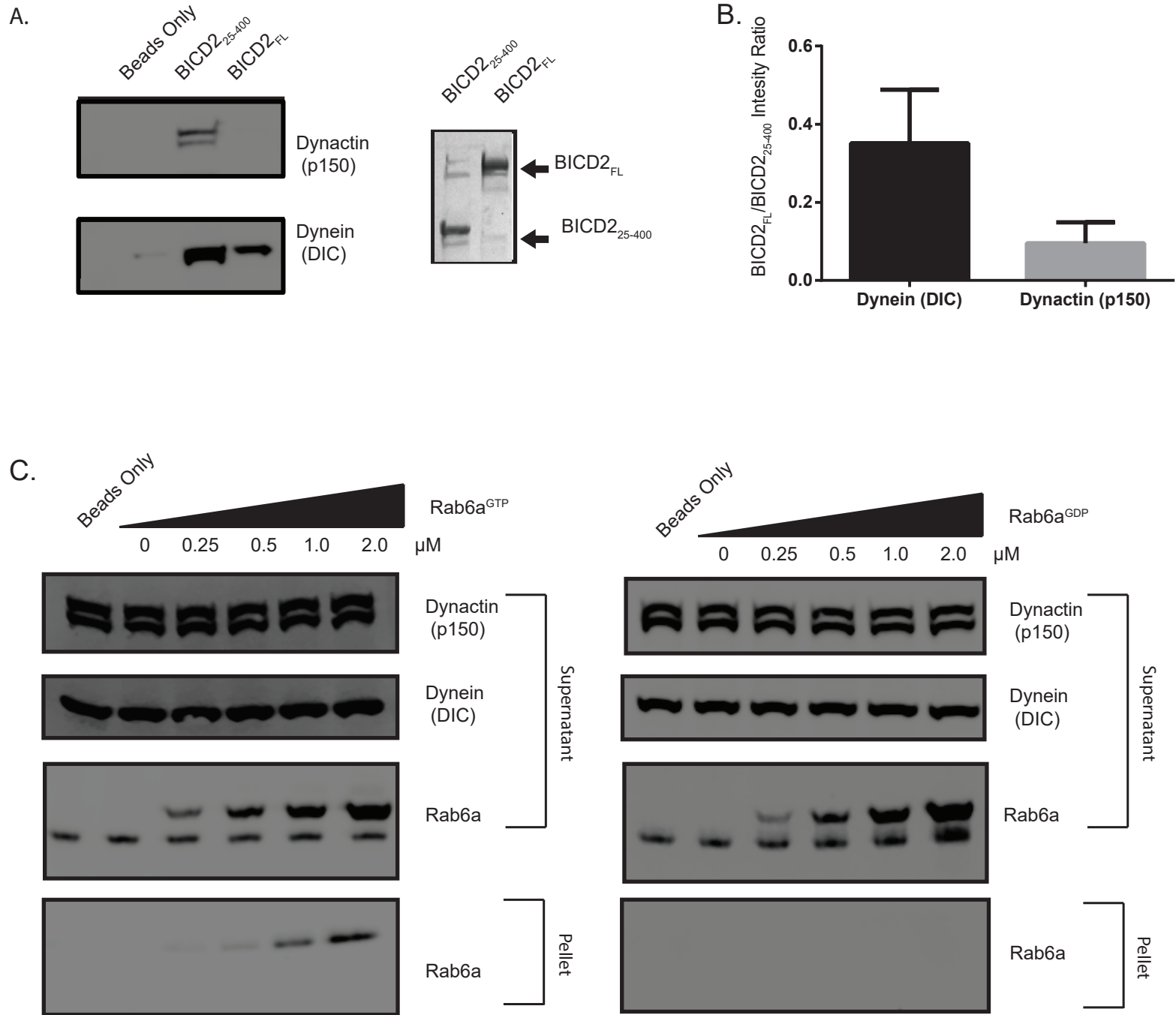
D.

Wildtype

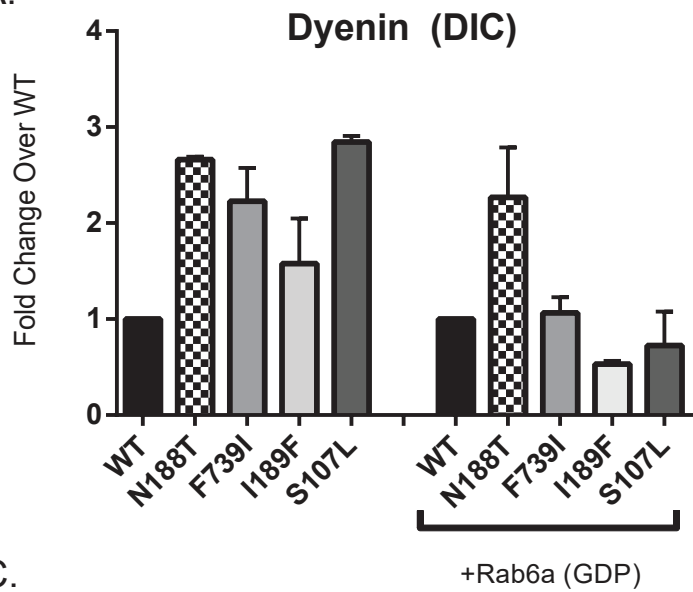


BICD2 Mutants

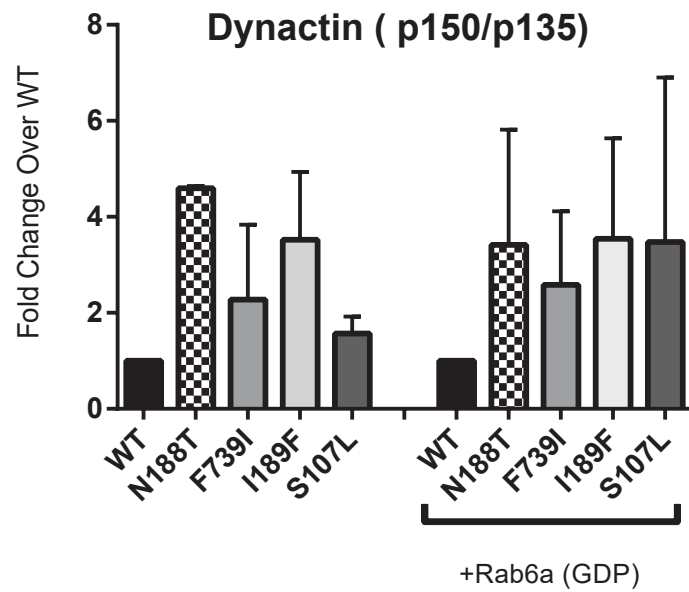




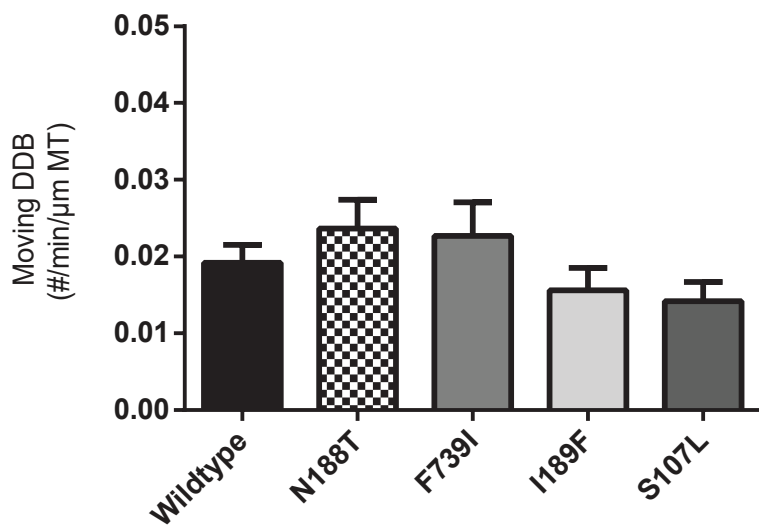
A.



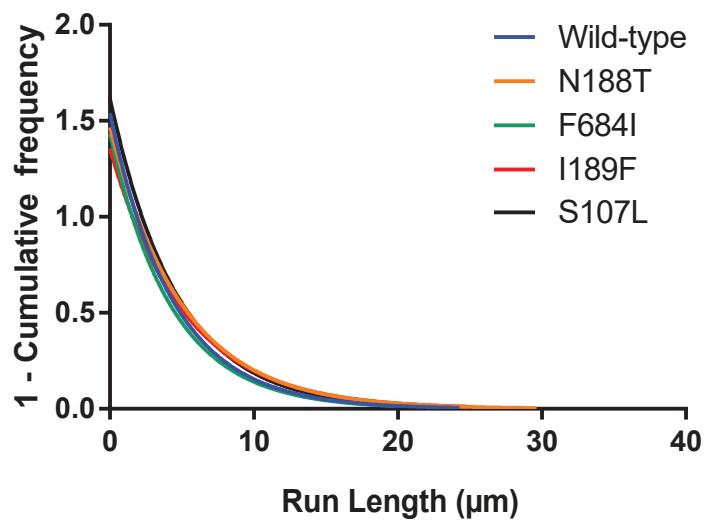
B.



C.



D.



E.

